SPECIAL
Air-sea interaction during PISTON-MISOBOB-CAMP2Ex
COLLECTION

# Observations of Eddy-Modulated Turbulent Mixing in the Southern Bay of Bengal

C. A. LUECKE,[a] H. W. WIJESEKERA,[a] E. JAROSZ,[a] D. W. WANG,[a] J. C. WESSON,[a] S. U. P. JINADASA,[b] H. J. S. FERNANDO,[c] AND W. J. TEAGUE[d]

[a] *Naval Research Laboratory, Stennis Space Center, Mississippi*
[b] *Ocean University, Colombo, Sri Lanka*
[c] *Department of Civil and Environmental Engineering and Earth Sciences, University of Notre Dame, Notre Dame, Indiana*
[d] *SRR International, Inc., Riviera Beach, Florida*

(Manuscript received 7 November 2020, in final form 6 March 2021)

ABSTRACT: Long-term measurements of turbulent kinetic energy dissipation rate ($\varepsilon$), and turbulent temperature variance dissipation rate ($\chi_T$) in the thermocline, along with currents, temperature, and salinity were made at two subsurface moorings in the southern Bay of Bengal (BoB). This is a part of a major international program, conducted between July 2018 and June 2019, for investigating the role of the BoB on the monsoon intraseasonal oscillations. One mooring was located on the typical path of the Southwest Monsoon Current (SMC), and the other was in a region where the Sri Lanka dome is typically found during the summer monsoon. Microstructure and finescale estimates of vertical diffusivity revealed the long-term subthermocline mixing patterns in the southern BoB. Enhanced turbulence and large eddy diffusivities were observed within the SMC during the passage of a subsurface-intensified anticyclonic eddy. During this time, background shear and strain appeared to influence high-frequency motions such as near-inertial waves and internal tides, leading to increased mixing. Near the Sri Lanka dome, enhanced dissipation occurred at the margins of the cyclonic feature. Turbulent mixing was enhanced with the passage of Rossby waves and eddies. During these events, values of $\chi_T$ exceeding $10^{-4}\,°C^2\,s^{-1}$ were recorded concurrently with $\varepsilon$ values exceeding $10^{-5}\,W\,kg^{-1}$. Inferred diffusivity peaked well above background values of $10^{-6}\,m^2\,s^{-1}$, leading to an annually averaged diffusivity near $10^{-4}\,m^2\,s^{-1}$. Turbulence appeared low throughout much of the deployment period. Most of the mixing occurred in spurts during isolated events.

KEYWORDS: Diapycnal mixing; Eddies; Fluxes; Ocean dynamics; Turbulence; Anticyclones; Rossby waves; Microscale processes/variability; Monsoons

## 1. Introduction

The southern Bay of Bengal acts as a critical link between the low-salinity northern part of the bay, and the high-salinity water of the Arabian Sea. Freshwater input from rivers and rainfall must be exchanged with high-salinity waters of the Arabian Sea to the south and west in order to maintain basin-scale mixing. Recent studies (e.g., Schott and McCreary 2001; Bhat et al. 2001; Webster et al. 2002; Rao et al. 2011; Wijesekera et al. 2016a; Vinayachandran et al. 2018) have highlighted the influence of oceanic–atmospheric coupling within the Bay of Bengal (BoB) on the onset and intensity of the Indian Ocean monsoon (IOM). Understanding the exchange of water masses and the associated heat and salinity fluxes that are driving factors for upper-ocean heat content and mixed layer structure of the BoB is of utmost importance to understand and predict the IOM. Subsurface mixing is likely to play an important role in sea surface temperature (SST) and salinity variability within the BoB. Quantification of mixing in the BoB is therefore critical for the understanding of water-mass exchange, and vertical transfer of heat and salinity between subsurface and surface waters. Forcing from the monsoon, coupled with energetic mesoscale and submesoscale features, complicates the regional circulation, and as a consequence, the mechanisms that drive turbulent mixing and water-mass exchange between the BoB and the Arabian Sea are poorly understood. Furthermore, details of how mixing processes regulate and influence air–sea interactions in the southern BoB are not well defined.

Within the BoB, the seasonal reversal of the winds due to the monsoonal cycle (Kumar et al. 2012) is the dominant seasonal feature that defines the large-scale circulation. From May through September, strong southwesterly winds impart wind stress-curl forces, spinning up the Southwest Monsoon Current (SMC), also known as the Summer Monsoon Current. During this time, a semistationary mesoscale cyclonic eddy known as the Sri Lanka dome (SLD) (Vinayachandran and Yamagata 1998; Lozovatsky et al. 2016; Cullen and Shroyer 2019) is formed to the east of Sri Lanka. October through November is a transitional period leading into the northeast monsoon during the months of December–February, while March and April are again transitional periods, marked by low winds.

The large-scale dynamics, forced by the IOM, generate a rich field of mesoscale and submesoscale motions, which, in turn, provide the mechanisms for turbulent mixing. Recent observations revealed the formation and propagation of eddies and Rossby waves in the southern BoB, and their interactions with

*Corresponding author*: Conrad A. Luecke, conrad.luecke.ctr@nrlssc.navy.mil

DOI: 10.1175/JPO-D-20-0280.1

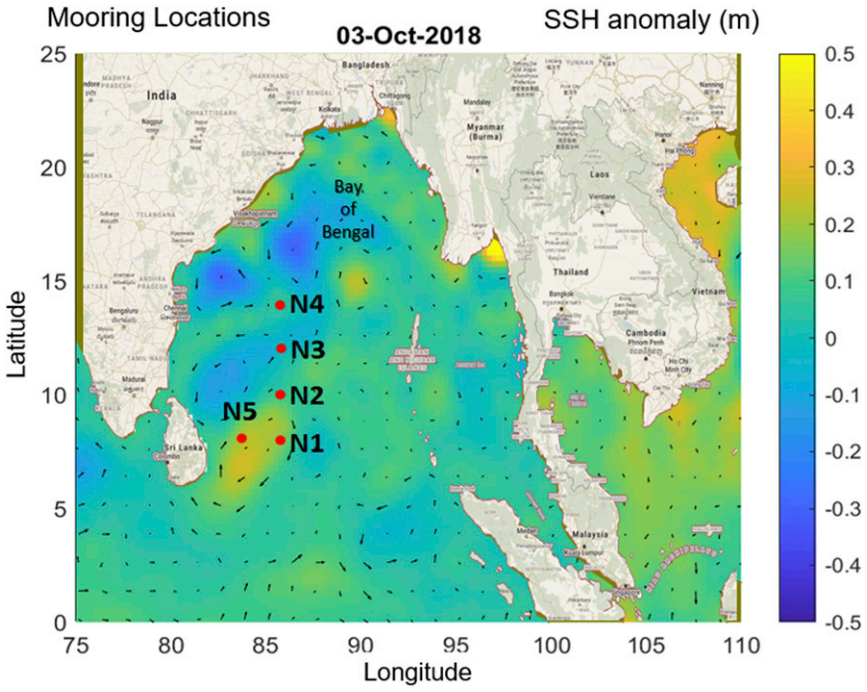


FIG. 1. Locations of moorings overlaid with SSH anomaly and geostrophic velocities from AVISO products (https://www.aviso.altimetry.fr/en/data/products.html). Moorings N1 and N5, the focus of this study, are contained within the black ellipse.

the SMC (Wijesekera et al. 2016b; Webber et al. 2018; Pirro et al. 2020a,b). Wijesekera et al. (2016b) noted that a cyclonic and anticyclonic eddy pair influenced the location and strength of the SMC during the summer of 2014. Webber et al. (2018) reported that the variability in SMC strength and position is driven by the combination of local forcing (wind stress curl over the Sri Lanka dome) and remote equatorial forcing (Kelvin and Rossby wave propagation). Pirro et al. (2020a) reported an anticyclonic eddy southeast of Sri Lanka in July 2018 with surface velocities up to $\sim 1\,\mathrm{m\,s^{-1}}$, a size in the meridional direction of $\sim 200\,\mathrm{km}$, and penetration approximately to the depth of the thermocline ($\sim 150\,\mathrm{m}$).

The complex and multiscale spatial–temporal geography of upper-ocean mixing in the Bay of Bengal has been the focus of several studies. Warner et al. (2016) observed heightened subsurface turbulence during the southwest monsoon, and during the passage of a storm. Cherian et al. (2020) found turbulent mixing below the mixed layer to be relatively weak throughout much of the year, with elevated signals during the southwest monsoon, and bursts of turbulence due to low-frequency current shear between October and January. Thakur et al. (2019) found a similar pattern of intermittent mixing in yearlong records to the north, which show variability in turbulence observed at diurnal, semidiurnal, and shorter time scales below the mixed layer. Microstructure surveys conducted off the east coast of Sri Lanka revealed relatively weak subsurface dissipation rates (Jinadasa et al. 2016); however, Lozovatsky et al. (2019) found locally elevated turbulence at the periphery of the SLD. A modeling study by Jensen et al. (2016, 2020) found that both the propagation of internal tides and stirring from the local eddy field may be significant mechanisms for mixing in the BoB, and recent mooring

TABLE 1. Summary of ADCP instruments on moorings N1 and N5. An instrument depth is given in meters. Up is for upward-looking and down is for downward-looking ADCP.

| Mooring | Lat | Lon | Water depth (m) | Instrument depth and orientation | Type (KHz) | Sampling rate | Bin size (m) |
|---|---|---|---|---|---|---|---|
| N1 | 8°0.1′N | 85°45.2′E | 3740 | 90 m up | 300 | 3 pings for 5 min every 1 h | 2 |
| | | | | 110 m up | 300 | 100 pings for 5 min every 1 h | 2 |
| | | | | 110 m down | 75 | 40 pings for 1 h | 8 |
| | | | | 710 m down | 75 | 40 pings for 1 h | 8 |
| N5 | 8°5.1′N | 83°43.1′E | 3815 | 90 m up | 300 | 3 pings for 5 min every 1 h | 2 |
| | | | | 110 m up | 300 | 100 pings for 5 min every 1 h | 2 |
| | | | | 110 m down | 75 | 40 pings for 1 h | 8 |
| | | | | 710 m down | 75 | 40 pings for 1 h | 8 |

observations of hydrographic and current data suggest that interactions between semidiurnal tides and eddies in the southern BoB are likely to enhance turbulent mixing in the thermocline (Wijesekera et al. 2019).

The question arises: given the relative intermittency of elevated turbulent mixing in the southern BoB, what are the key mechanisms behind the subsurface mixing necessary to balance the freshwater input associated with the monsoon? It has been suggested that the southern BoB is a region where enhanced mixing occurs (Vinayachandran et al. 2013); however, it remains unknown how the mesoscale eddy field influences mixing. The aim of the work presented here is to understand the mechanisms of water-mass exchange between the BoB and the Arabian Sea through the context of yearlong, subsurface dissipation estimates from moorings. We focus on a period of mooring deployment from July of 2018 through May of 2019. Long-term measurements of turbulent kinetic energy (TKE) dissipation rates ($\varepsilon$) and temperature variance dissipation rates ($\chi_T$) provide insight into the intermittent nature of mixing at the base of the thermocline in the BoB. Velocity and hydrographic data from two subsurface moorings, each equipped with fast thermistors and microstructure shear probes, are used to quantify $\varepsilon$ and $\chi_T$, and to investigate the role of monsoon-driven mesoscale dynamics on mixing. We observe significantly enhanced turbulence during the passage of a subsurface-intensified anticyclonic eddy. During this time, background shear and strain appear to lead to the increased turbulent vertical heat flux.

Yearlong records of turbulence help to bridge the gap between ship-based microstructure surveys, which are typically limited in duration, and studies that focus on larger-scale dynamics through the use of remote sensing, modeling, and mooring arrays. This work attempts to frame the small-scale turbulent dissipation within a larger framework of mesoscale motions in the BoB. Turbulent dissipation rates along with velocity and hydrographic fields were collected as a part of the U.S. Naval Research Laboratory (NRL) research initiative, Role of Indian Ocean on Monsoon Intraseasonal Oscillations (RIO-MISO), which was conducted in collaboration with another research initiative, Oceanic Control of Monsoon Intraseasonal Oscillations in the Tropical Indian Ocean and the Bay of Bengal (MISO-BOB), sponsored by the U.S. Office of Naval Research (ONR). Together, this work is aimed at furthering the understanding of the role of the ocean in modulating the propagation of the monsoon intraseasonal oscillations in the BoB. The observational program includes long-term mooring observations, shipboard oceanic and atmospheric measurements, and autonomous vehicle measurements. Here, we focus on turbulent mixing in the thermocline, below the mixed layer, at semidiurnal to seasonal time scales, exploring how the upper ocean/thermocline influences MISO cycles and monsoon development.

The paper is organized as follows. The moorings and data, as well as the methodology used for our turbulence measurements, are described in section 2. In section 3, background flow conditions such as the SMC, Rossby waves, and eddies are described. In section 3, we also highlight current variability on time scales such as tidal, inertial, and subseasonal, which are identified from wavelet and conventional spectral methods. In section 4, we present shear and temperature microstructure measurements, along with estimates of diffusivity based on finescale parameterizations. Additionally, we use temperature and salinity measurements in conjunction with the microstructure data to estimate turbulent heat and salinity fluxes. Conclusions are presented in section 5.

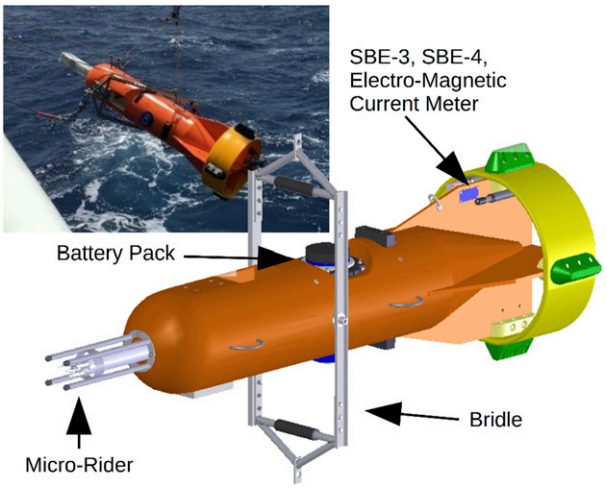


FIG. 2. Diagram of the MicroMoor float. Arrows show the position of the MicroRider (microstructure package described in the text), battery pack, and secondary SBE temperature/salinity sensors. In the photo, the MicroRider is protected by a tubular cover with a burn wire released within a day of deployment. Illustration provided by Rockland Scientific Inc.

## 2. Instrumentation, observations, and methods

As a component of the MISO-BOB campaign, five subsurface moorings were deployed in the Bay of Bengal from July 2018 to June 2019. The spatial layout of the moorings is shown in Fig. 1. These moorings were designed to collect both current and hydrographic data. For the purpose of this study, we focus on two of these moorings, N1 and N5 (Fig. 1), because in addition to the temperature, conductivity, and current velocity instruments, these moorings were equipped with instrumentation to collect both shear- and temperature-based turbulent microstructure observations. Horizontal currents were measured using 300-kHz acoustic Doppler current profilers (ADCPs) for the upper water column, and 75-kHz ADCPs to extend coverage at depth. ADCP locations and details for N1 and N5 can be found in Table 1. The ADCPs provided high-quality velocity data; however, a portion of the upper-water-column velocity data between 115 m and the sea surface was lost at N5 after 14 February 2019 due to instrument failure. For calculations in this paper, hourly velocity data were interpolated to an 8-m grid between depths of 30 and 1200 m.

A combination of instruments was used to measure temperature ($T$), conductivity ($C$), and pressure ($P$). SBE37 ($T$, $C$, $P$), SBE39 ($T$, $P$), SBE56 ($T$), Vemco ($T$), and RBR solo [dissolved oxygen (DO)] sensors were installed at approximately

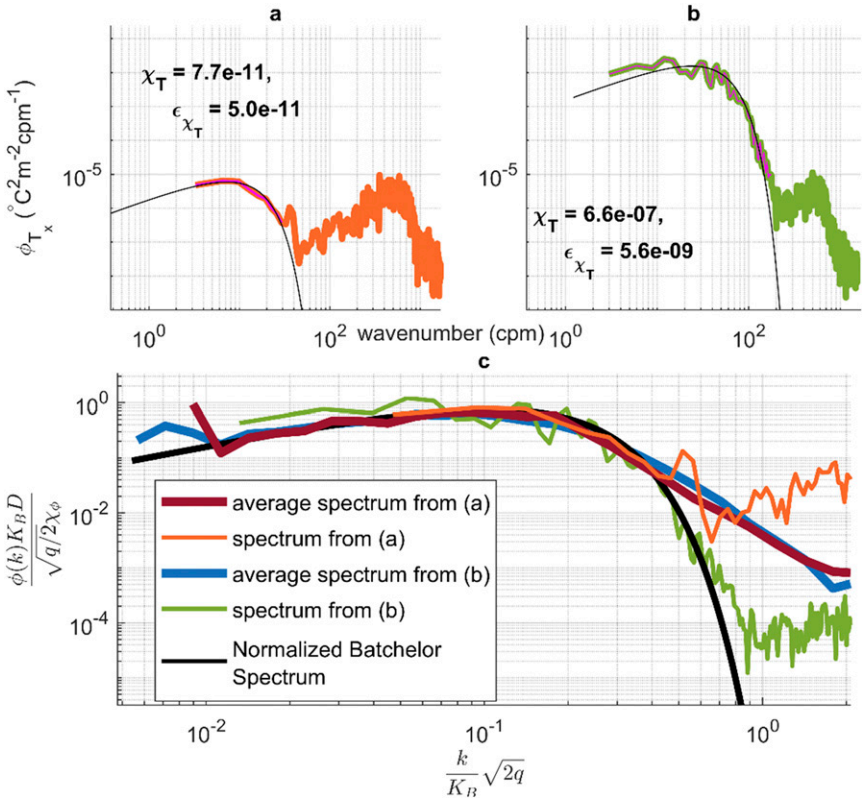


FIG. 3. Examples of temperature gradient wavenumber spectrum (orange and green lines) from a thermistor attached to the MicroMoor/MicroRider package. (a) The spectrum depicts a period of relatively weak turbulence. (b) The spectrum depicts a period of strong turbulence. The thin black lines are the fitted theoretical Batchelor spectrum. (c) Both spectra in nondimensional form, along with spectra averaged over the 10-min period from which each example in (a) and (b) was taken. The $\chi_T$ estimates are in units of °C$^2$ s$^{-1}$, and TKE dissipation rates $\varepsilon_{\chi_T}$ derived from $\chi_T$ are in W kg$^{-1}$.

5 m intervals between the top of the moorings and a depth of ~ 130 m, at 10-m intervals to 230 m, and at larger intervals in deeper water (Table 1). Two MicroMoors (Fig. 2), for measuring shear microstructure and high-frequency temperature, were located on moorings N1 and N5 in the thermocline, below the mixed layer at approximately 105 and 145 m, respectively. The MicroMoor is a 4.5-m-long instrument platform, with a weight of 282 kg and a net positive buoyancy of 166 kg (e.g., https://rocklandscientific.com/products/moored-systems/nemo/). The MicroMoor was attached to the mooring line via a swivel and bridle on both the top and bottom. The bridle acts as a pivot and permits the MicroMoor to remain level during mooring blowdown. The MicroMoor carries three main instrument systems; first, a Rockland Scientific (RSI) MicroRider turbulence sensor package located in the nose section of the float and consists of two air-foil shear probes, and two FP07 fast thermistors. Velocity-shear and acceleration measurements were taken continuously at 512 Hz for 10 min every hour. Temperature pressure, tilt, and yaw sensors along with a magnetometer recorded instrument orientation at 256 Hz. Reference temperature and conductivity were measured via a tail-mounted Sea-Bird Electronics (SBE) 3 temperature sensor and SBE 4 conductivity cell. Third, an electromagnetic current meter mounted on the tail of the instrument provided horizontal current velocity. Due to issues relating to vehicle pitch, ADCP velocities were used in the computation of horizontal wavenumbers in this paper. All these datasets, excluding the ADCP velocities, were recorded inside the MicroRider. Further details of the MicroMoor float are given in Lueck et al. (2015). The shear probes are used to determine the TKE dissipation rate $\varepsilon$, while the high-frequency temperature time series are used to compute the horizontal temperature gradient. Temperature gradient spectra are then integrated in order to determine the temperature variance dissipation rate $\chi_T$.

### a. *Microstructure processing*

Velocity shear and temperature measurements were processed using software provided by Rockland Scientific (Lueck 2016). We provide a brief overview of this processing here. A comprehensive explanation of the data processing algorithms and procedures are available in RSI's Technical Note 028 (Lueck 2016). We estimate the variance from the measured shear and temperature gradient spectra record in half-overlapping 8-s segments. Each of these is further subdivided into three half-overlapping 4-s subsegments, which are detrended, cosine windowed, and transformed into shear

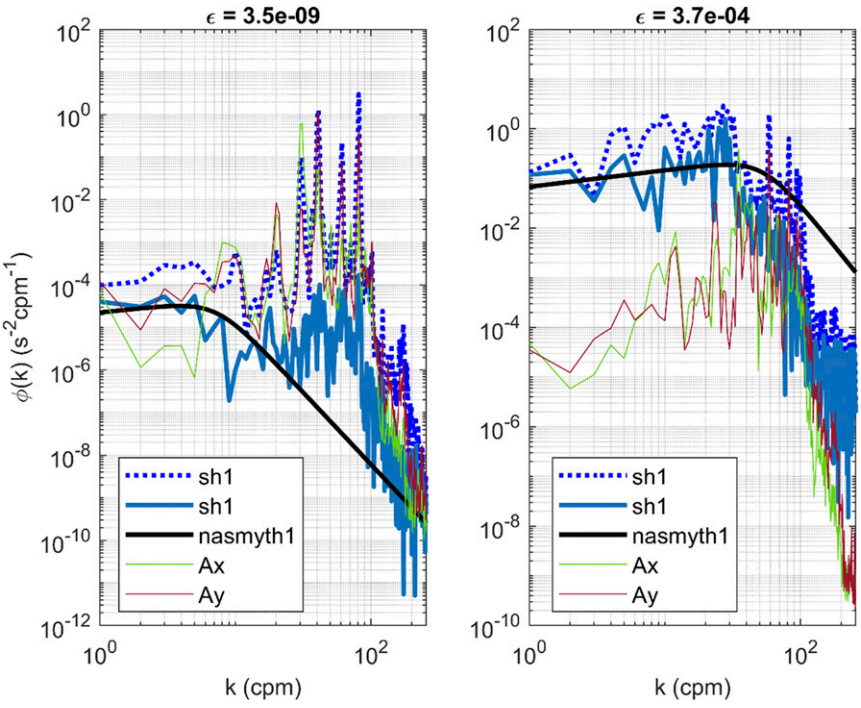


FIG. 4. The wavenumber spectra of two orthogonal components of the shear from the MicroMoor/MicroRider package during a period of (left) low and (right) high turbulence. Clean shear spectra are shown with blue lines. The dotted blue lines are the spectra prior to coherent-noise removal. The thin green and red lines show the spectra of acceleration used to remove noise. The dimensional Nasmyth spectra are depicted by solid black lines for the estimated rate of TKE dissipation (W $kg^{-1}$) listed above each plot.

power spectra using a fast Fourier transform (FFT). Each set of the three spectra is averaged to create a single shear or temperature gradient power spectra. Coherent acceleration signals are removed from the shear spectra using the Goodman et al. (2006) algorithm. This spectral processing was chosen to best eliminate the effects of an apparent 10-s vertical oscillation observed on the MicroMoor platform. Both shear and temperature-gradient frequency spectra are transformed into wavenumber ($k$) space using current velocities from the ADCP instrument for each 10-min MicroMoor data segment and assuming Taylor's frozen-field hypothesis is $k = \omega/U$, where $\omega$ is the frequency and $U$ is the flow speed relative to the sensor. Because of ballasting issues of the MicroMoor, the float tilted upward during the low velocity flow; hence, our calculation of TKE dissipation rates were limited to periods with the current velocity above 0.15 $m s^{-1}$, and an instrument pitch angle of less than 15°. Shear spectra are fitted to Nasmyth spectra (e.g., Nasmyth 1970; Wolk et al. 2002) and integrated, providing an estimate of the TKE dissipation rate $\varepsilon$:

$$\varepsilon = \frac{15}{2}\nu\int_0^\infty \Psi(k)\,dk, \tag{1}$$

where $\Psi(k)$ is the wavenumber spectrum of horizontal shear (Lueck 2016; Osborn 1974) and $\nu$ is the kinematic viscosity of seawater. In practice, an upper integration limit is necessary to exclude electronic noise which dominates the spectra at large wavenumbers. A third-order polynomial was fit to the shear spectra in order to determine the location of the spectral minimum, an indicator for the onset of noise domination (Lueck 2016). Conversely, high-frequency gradient spectra are integrated to provide an estimate of the rate of temperature variance dissipation $\chi_T$:

$$\chi_T = 6D\int_0^\infty \phi_{Tx}(k)\,dk, \tag{2}$$

where $\phi_{Tx}$ is the temperature gradient wavenumber spectra (Dillon and Caldwell 1980; Moum and Nash 2009) and $D$ is the thermal diffusivity. To better resolve temperature microstructure, we limit our estimates of $\chi_T$ to periods where the current magnitude is below 0.25 $m s^{-1}$. Temperature gradient spectra are integrated between 0.5 and 10 Hz. Temperature gradient spectra are also iteratively fit to the theoretical Batchelor spectrum (Batchelor 1959). We find both methods of determining $\chi_T$ produced similar results and, for the purposes of this paper, only present estimates based on the iterative fits to the theoretical Batchelor spectrum. We then estimate eddy diffusivity using $\chi_T$ and $\varepsilon$, respectively:

$$K_T = \frac{\chi_T}{2T_z^2}, \tag{3}$$

$$K_\rho = \frac{\Gamma\varepsilon}{N^2} \tag{4}$$

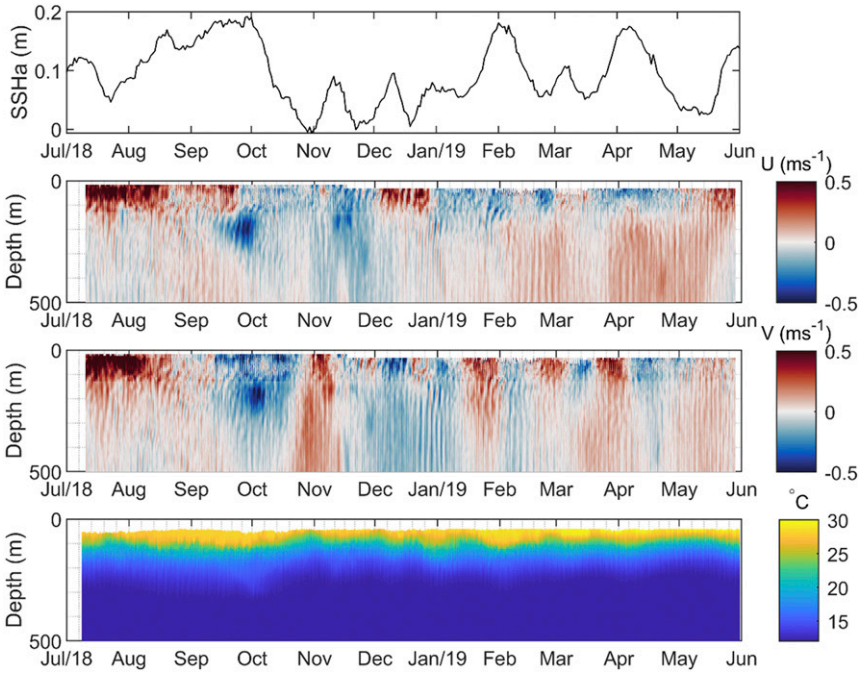


FIG. 5. Time series of AVISO sea surface-height anomaly (SSHa), depth profiles of current zonal ($U$) and meridional ($V$) velocities, and temperature as a function of depth and time at N1.

(Osborn and Cox 1972; Osborn 1980), where $T_z$ is the local vertical temperature gradient determined from the temperature sensors on the mooring line, the mixing efficiency of $\Gamma = 0.2$ (Gregg et al. 2018), and $N$ is the buoyancy frequency calculated using CTDs on the mooring line. Sample temperature-gradient and shear spectra are shown in Figs. 3 and 4. In the top two panels of Fig. 3, observed temperature spectra are overlaid with the theoretical Batchelor fit (black curve) (e.g., Dillon and Caldwell 1980). The upper-left panel shows a temperature gradient spectrum from a period of low

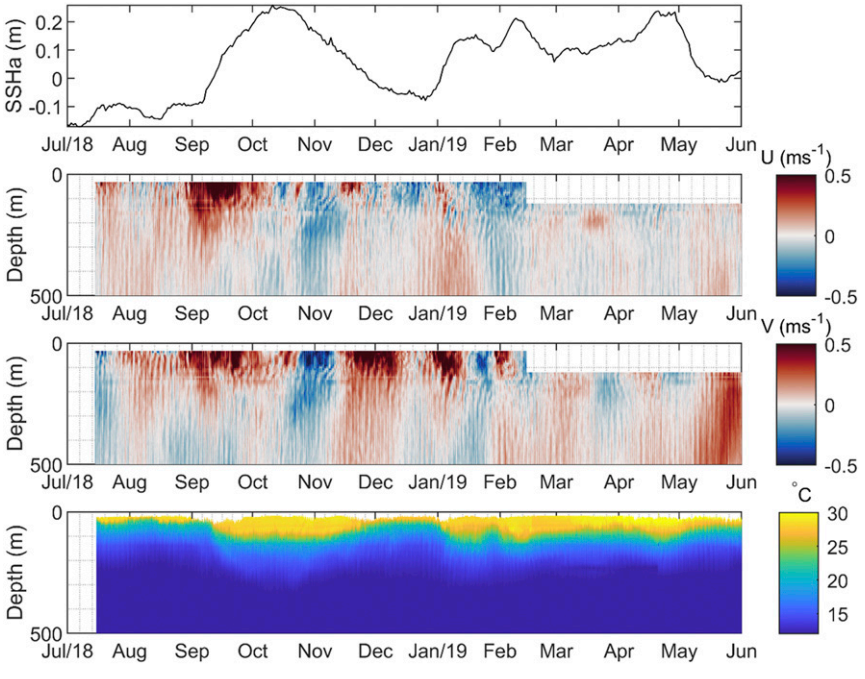


FIG. 6. As in Fig. 5, but for N5.

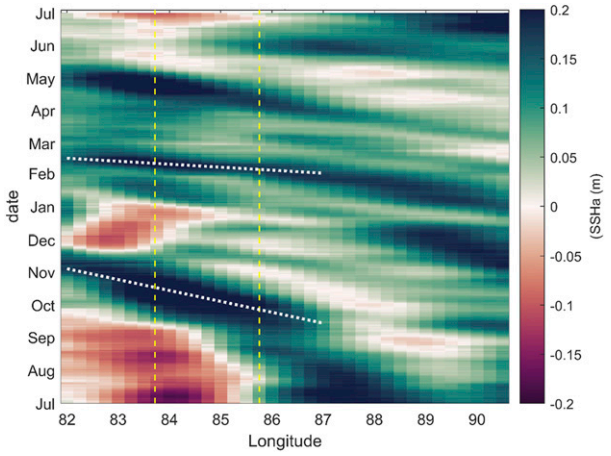


FIG. 7. SSH anomaly from AVISO at the approximate latitude of N1 and N5 plotted along the longitude range (82°–91°E). Dotted white lines represent propagation speeds of 0.45 $ms^{-1}$ during February–March 2019 at 82°–87°E (top line) and 0.12 m $s^{-1}$ during September–November 2018 at 82°–87°E (bottom line). Vertical dashed lines indicate the longitudes of N1 (right line) and N5 (left line).

turbulence, and the right shows spectrum during a more energetic period. The portion of the observed spectra highlighted in magenta represents the area to be fit to determine $\chi_T$. In the bottom panel, both spectra are shown in nondimensional form, as in Dillon and Caldwell (1980), where $q = 3.9$, and $k_b = (\varepsilon\nu^{-1}D^{-2})^{1/4}$ is the Batchelor wavenumber. In Fig. 4, shear spectra are overlaid with Nasmyth curves (e.g., Nasmyth 1970; Wolk et al. 2002). The thick blue curves show the denoised shear spectra, while the black lines show Nasmyth spectra. The panels on the left depict spectra taken from a time of relatively weak turbulent mixing, while the right panels show spectra during periods of stronger turbulence.

### b. *Finescale mixing estimates*

To provide an estimate of mixing rates independent from those evaluated from the microstructure measurements on the MicroMoor platform, we employ an empirically derived finescale parameterization of the eddy diffusivity based on internal-wave statistics (Polzin et al. 1995; Kunze 2017; Wijesekera et al. 2019):

$$K = K_0 \left( \frac{\langle \lambda_{10}^2 \rangle^2}{\langle \lambda_{10\mathrm{GM}}^2 \rangle^2} \right) h(R_w) j\left(\frac{N}{f}\right), \tag{5}$$

where $K_0$ is the background eddy diffusivity of $0.05 \times 10^{-4}$ $m^2$ $s^{-1}$, $\lambda_{10}^2$ and $\lambda_{10\mathrm{GM}}^2$ are the internal-wave strain variance estimated from the mooring at a 10-m vertical scale using a semi-Lagrangian approach (e.g., Wijesekera et al. 1993), and from the Garret–Munk internal-wave spectrum, respectively, where $f$ is the inertial frequency. The 10-m vertical spacing was selected in order to be consistent with previous studies (e.g., Gregg 1989). Here, 10-m strain is estimated from the moored temperature sensors, where $\lambda_{10} = (\eta_n - \eta_{n+1})/10$, and $\eta_n$ and $\eta_{n+1}$ are the vertical displacements of two isotherms from their 7-day time-averaged depths. The mean vertical shear-squared is estimated on 10-m vertical scales as

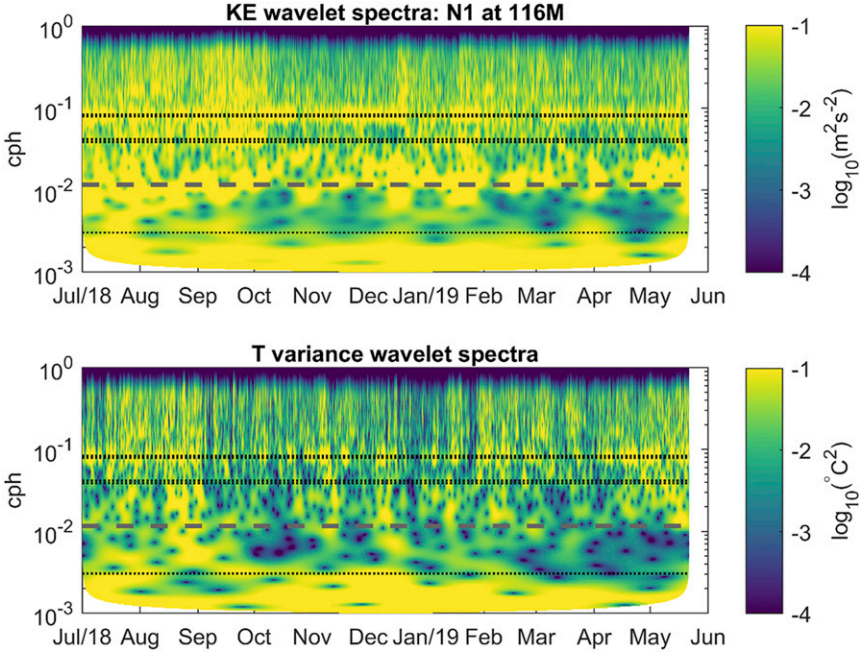


FIG. 8. The wavelet variance spectra of (top) velocity and (bottom) temperature at a depth of 116 m at N1. In both subplots, the horizontal black lines indicate (from top to bottom) semidiurnal, diurnal, inertial, and spring–neap periods.

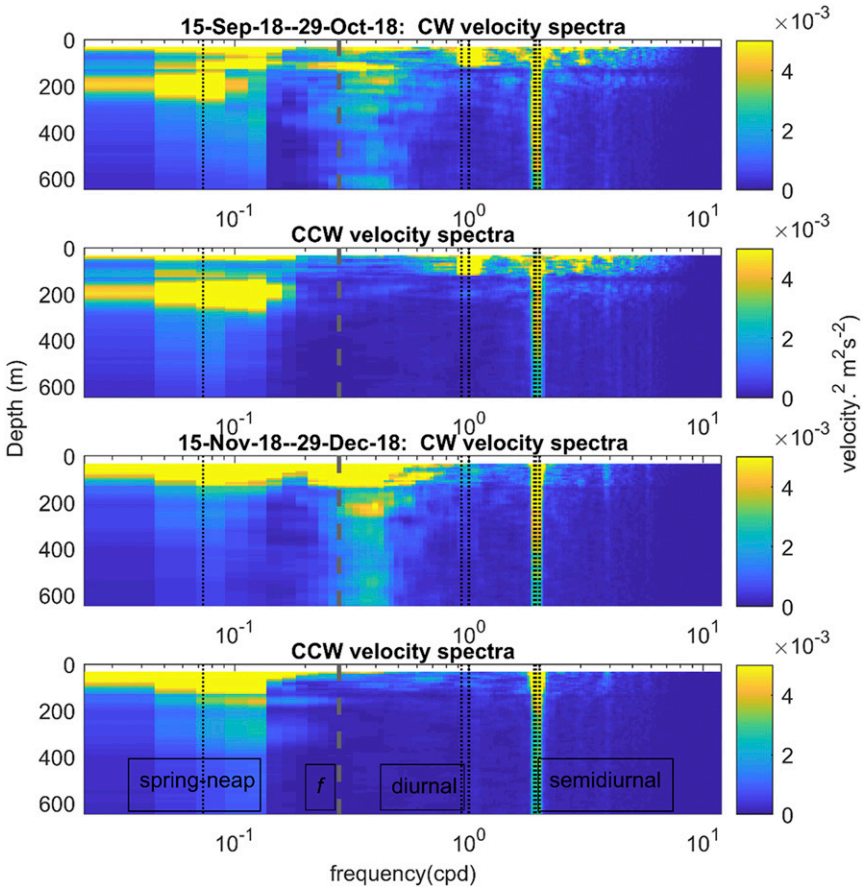


FIG. 9. Variance preserving depth–frequency rotary spectra of velocity at N1. (top two panels) Clockwise (CW) and counterclockwise (CCW) spectra during the occurrence of an energetic, anticyclonic eddy, and (bottom two panels) the CW and CCW spectra for the period after the passage of the eddy, taken one month later. The vertical black lines (from left to right) indicate spring–neap, inertial, diurnal ($K_1$, $O_1$), and semidiurnal ($M_2$, $S_2$) periods.

$\mathrm{sh}^2 = 2.11[(du^2/dz) + (dv^2/dz)]$, where $du/dz$ and $dv/dz$ represent the zonal and meridional components of the velocity gradient, and the 2.11 multiplier acts as a correction factor for the first difference filter corresponding to the Garret–Munk spectrum (e.g., Gregg 1989; Gregg and Sanford 1988). The ratio of shear to strain variances is

$$R_w = \mathrm{sh}^2/(N^2\lambda_{10}^2), \tag{6}$$

and the function $h(R_w)$ describes the dependence of the shear-to-strain ratio:

$$h(R_w) = \frac{1}{6\sqrt{2}} \frac{R_w(R_w+1)}{\sqrt{(R_w-1)}}, \tag{7}$$

while $j(f/N)$ represents the dependence of the ratio of the buoyancy to inertial frequency given by

$$j(f/N) = \frac{f \operatorname{arccosh}\left(\frac{N}{f}\right)}{f_{30} \operatorname{arccosh}(N_0/f_{30})}. \tag{8}$$

Because the function $h(R_w)$ approaches a singularity as $R_w$ approaches 1, we discard ~2% of the data for which values of $R_w$ goes below 1.1. In practice, we chose to calculate $R_w$, because we have the data available to do so; however, the results we present here are not changed significantly if $R_w = 3$ as in Whalen et al. (2015). We found the average values of $R_w$ at the depth of the MicroMoor to be 6.2 and 6.7, respectively, which is close to the value of 7 reported in Kunze et al. (2006). The finescale parameterization of eddy diffusivity, unlike the direct measurements made by the MicroMoor platform, are not limited to a specific depth and can be made throughout the water column where there is sufficient coverage of temperature, conductivity, and velocity.

## 3. Background flow characteristics

Figures 5 and 6 show AVISO sea surface height (SSH) and velocity and temperature at moorings N1 and N5, respectively, during the mooring deployment period. Both N1 and N5 exhibit a host of strong dynamical features. At N1, during August, the SMC penetrates to a depth of 150 m. As the

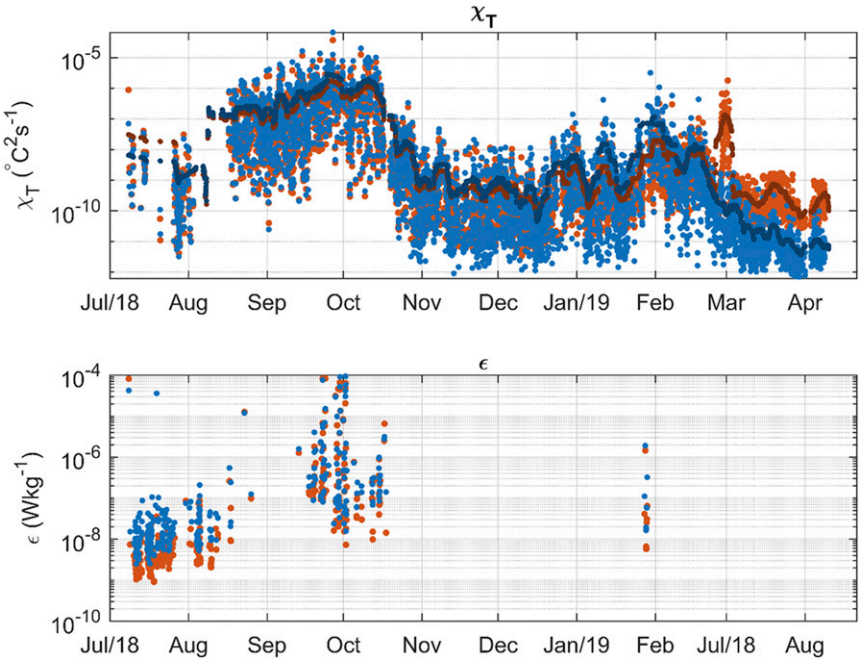


FIG. 10. Time series of (top) the temperature variance dissipation rate $\chi_T$ (°C$^2$ s$^{-1}$) and (bottom) the turbulent kinetic energy dissipation rate $\varepsilon$ (W kg$^{-1}$) at mooring N1. The red and blue markers represent 10-min averages of $\chi_T$ and $\varepsilon$, respectively, estimated for each individual thermistor and shear probe contained on the MicroMoor. The darker color dots represent a moving 3-day average of $\chi_T$.

southwest monsoon spins down, both moorings exhibit periodic low-frequency flow reversals. These reversals occur on time scales of 20–40 days, and are consistent with the signature of westward-propagating Rossby waves and eddies (Vinayachandran and Yamagata 1998; Chen et al. 2017). The passage of these eddies/Rossby waves appears as a vertical banding in the meridional and zonal components of the current velocity in Figs. 5 and 6 with periods ranging from a few weeks to a month. Two eddy-like surface features appear in the signals at N1 and N5 during summer. One is a large anticyclonic eddy to the southeast of Sri Lanka, which is expressed as a positive SSH anomaly (SSHa) at N1, and the other is an adjacent cyclonic eddy, referred to as the Sri Lanka dome, to the east of Sri Lanka, which can be seen by the negative SSH anomalies at N5. During the period from September through October, the eddy at N1 exhibits a subsurface-intensified velocity core with the highest velocity (~0.7 m s$^{-1}$) occurring at a depth of ~200 m. The Sri Lanka dome is constricted between eastern Sri Lanka and the central BoB, and appears to move northward during the encroachment of the anticyclonic eddy. A Hovmöller diagram for AVISO SSHa (Fig. 7) clearly shows the westward propagation of the low-frequency features apparent in the velocity sections (Figs. 5 and 6). Westward-propagating features during July and August are noted in Pirro et al. (2020a), and are consistent with topographically trapped Rossby waves; however, their occurrence is somewhat earlier than the signals described in this paper, which appear during September and November.

To further illustrate variability over time, a continuous wavelet transform (Torrence and Compo 1998) was performed at N1 for currents and temperature at a depth of 116 m. Figure 8 shows kinetic energy (top panel), and temperature variance wavelet spectra. The intermittent nature of high-frequency motions throughout the year can clearly be seen, where increases in kinetic energy (KE) appear in ''burst'' events. Although dominant persistent features can be seen at semidiurnal and near-inertial periods for KE and at semidiurnal periods for temperature variance, there is considerable variation over time. During periods of increased variance at these frequency bands, elevated variance appears to extend to higher frequencies, filling out the internal–gravity wave spectrum between $f$ and $N$.

During September–October, a subsurface intensified energetic anticyclonic eddy is observed at N1. The eddy is visible as a positive SSHa on 3 October 2018 (Figs. 1 and 5, top panel). High-frequency KE appears to be elevated during this time; however, the strongest high-frequency temperature variance appears to occur somewhat earlier during September. The mixed layer depth is 80–100 m during September and October, then decreases in depth during October, reaching a minimum depth at the beginning of November of around 50 m. The deepening of the thermocline during the anticyclonic eddy may explain the decreased high-frequency temperature variance seen during this time, as variations in temperature may be underresolved if the instrument is located within the transition to the mixed layer.

High-frequency motions such as near-inertial oscillations and semidiurnal and diurnal tides can be seen intermittently at both N1 (Fig. 8) and N5 (not shown). At these frequencies,

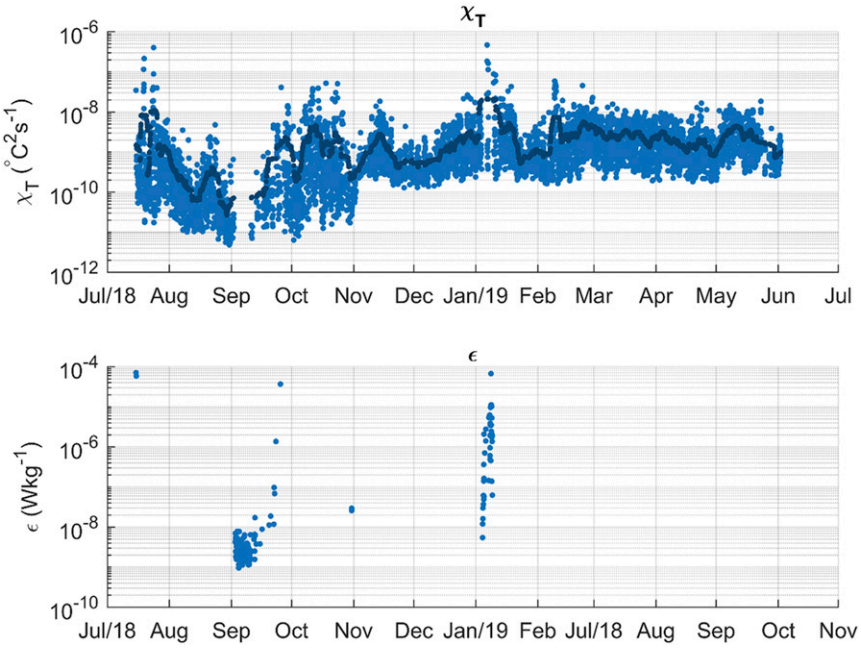


FIG. 11. As in Fig. 10, but for N5. Due to probe failures, only estimates from one thermistor and one shear probe are shown.

there is a high degree of temporal variability in velocity. Figure 10 shows area-preserving frequency–depth rotary spectra of the velocity at N1, taken about one month apart. During the period of 15 September–29 October 2018, variance in the anticyclonic eddy is elevated at both diurnal and semidiurnal frequencies, and the entire internal–gravity wave spectrum is elevated approximately to a depth of 100 m. Additionally, the semidiurnal band is elevated to about a depth of 500 m. Semidiurnal energy is higher at depths below 200 m in the clockwise component than in the counterclockwise component. A low-frequency subsurface maximum corresponding to the depth of the eddy can clearly be seen around 200 m at frequencies below $f$, from 0.03 to 0.1 cpd. In contrast, roughly one month later (15 November–29 December 2018, Fig. 9), the velocity spectra show weaker energetics at diurnal frequencies, and elevated variance in the semidiurnal band to a depth of 400 m. During both periods, the clockwise velocity spectra have near-surface elevated peaks around $f$, indicating downward-propagating near-inertial motions.

## 4. Observations of turbulent mixing

Estimates of long-term turbulence are presented in three ways. First, we present 10-min averages, taken at hourly intervals of the turbulent temperature variance dissipation rates and turbulent kinetic energy dissipation rates, from the MicroMoor instrumentation located on N1 and N5 (Figs. 10 and 11, respectively). Next, we present estimates of diffusivity calculated using a finescale parameterization at N1 and N5 (Figs. 14 and 16) down to 500 m. Last, we present long-term estimates of diffusivity using the MicroMoor-derived $\chi_T$ and $\varepsilon$ values according to Eqs. (3) and (4). We then compare diffusivity estimates made from finescale parameterizations to the microstructure diffusivity estimates (Figs. 15 and 17).

### a. Mixing estimates from microstructure

Long-term microstructure measurements revealed a highly intermittent mixing field, characterized by long periods of low $\chi_T$, punctuated by bursts of intense mixing. At N1 (Fig. 10), values of the temperature variance dissipation rate peak at $10^{-6}\,°C^2\,s^{-1}$ from September through October, during the passage of an anticyclonic subsurface-intensified warm-core eddy discussed previously. At N5 (Fig. 11), the temperature variance dissipation rates are lower than at N1, with peak values of $\chi_T$ of about $10^{-7}\,°C^2\,s^{-1}$ occurring in January. Likewise, the TKE-dissipation rate peaks at around $\varepsilon = 10^{-4}\,W\,kg^{-1}$ and $\varepsilon = 10^{-5}\,W\,kg^{-1}$ at N1 and N5, respectively.

The elevated dissipation during the anticyclonic subsurface-intensified eddy in October results in increased turbulent diffusivity. During this period, elevated subsurface mixing appears to coincide not only with the passage of the anticyclonic eddy, but also with heightened levels of the high-frequency velocity variance (Figs. 7–9). This indicates that the observed mixing event may not be only related to the eddy-induced straining of the background field but also to nonlinear interactions with higher-frequency motions within the eddy itself, such as internal tides and downward-propagating near-inertial waves (e.g., Polzin 2010; Kunze et al. 1995).

### b. Comparison with mixing estimates from finescale dissipation models

Finescale estimates are made from shear and strain based on internal-wave statistics as described earlier in the manuscript [Eqs. (5)–(8)]. Because our estimates of the strain field are

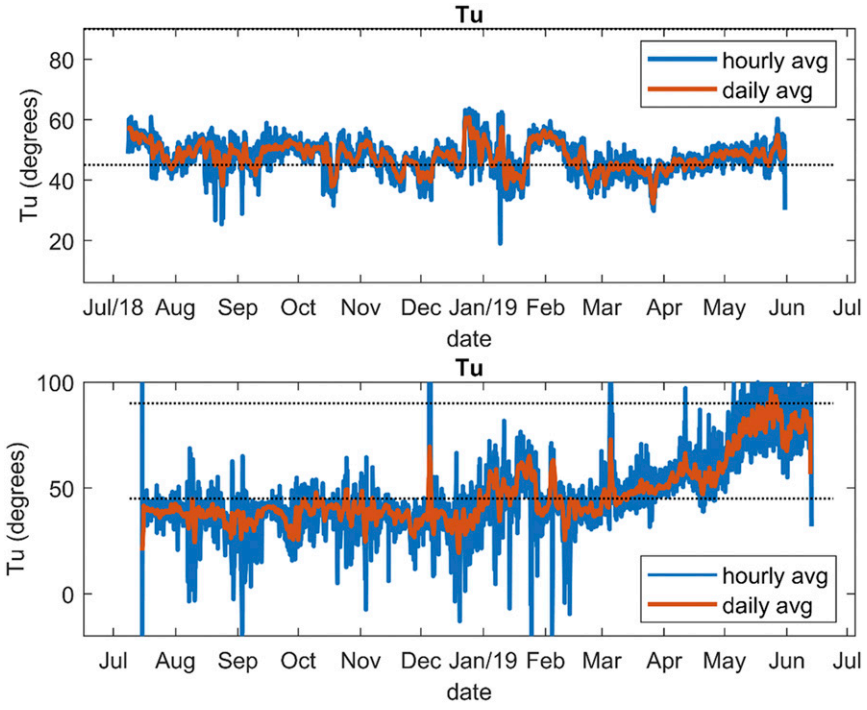


FIG. 12. Turner angle (Tu) computed at the depth of the MicroMoors for moorings (top) N1 and (bottom) N5. Hourly averages are shown in blue, and daily averages are in red. Horizontal dashed lines represent Tu = 45°, and Tu = 90°, respectively.

based on temperature, care must be taken to examine the relative contributions of salinity to density. In regions where salinity dominates, density may cause inaccuracies in our finescale strain estimates based on temperature. Because of this, we first present an analysis of the Turner angle (Ruddick 1983) at the depth of the MicroMoors at both N1 and N5 (Fig. 12). The Turner angle provides a way for estimating the relative contributions of temperature and salinity on density.

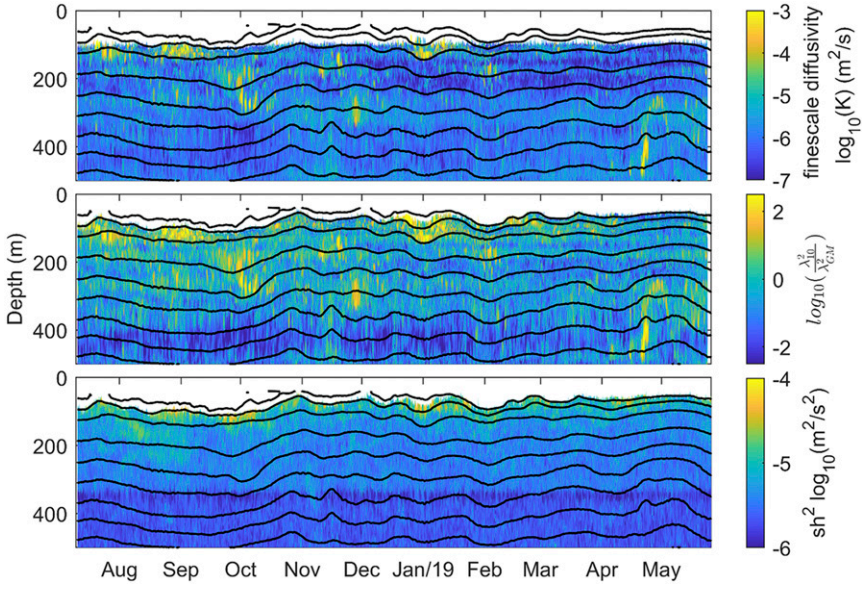


FIG. 13. Finescale (top) eddy diffusivity, (middle) strain ratios, and (bottom) shear calculated at N1. The black lines are 5-day low-passed isotherms drawn approximately every 50 m.

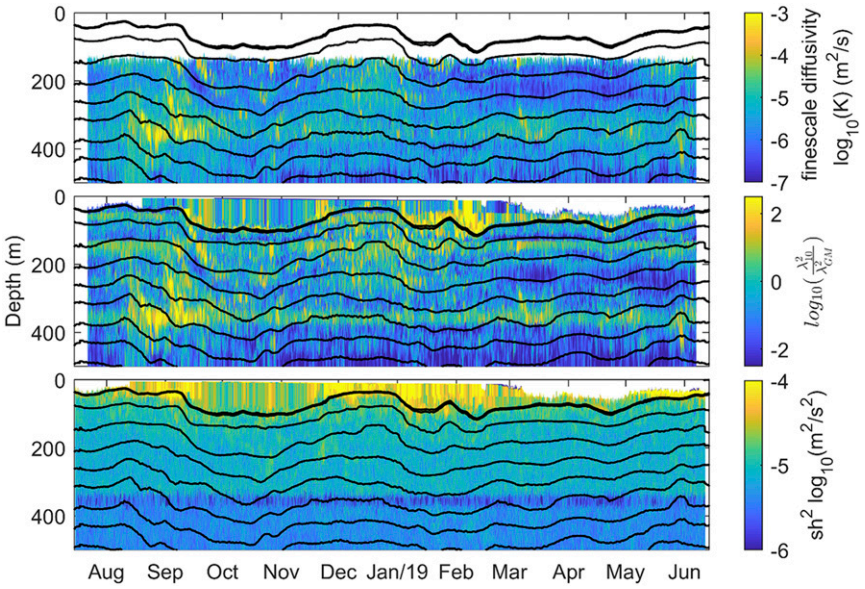


FIG. 14. As in Fig. 13, but for N5.

If the Turner angle is near 45°, the salinity contribution to density is negligible. For a Turner angle between 0° and 45° and between 45° and 90°, the salinity contribution increases, but temperature still dominates. Results for both N1 and N5 indicate that the use of temperature to estimate strain is valid for most of the deployment; however, from April through the end of the deployment, the Turner angle at N5 reaches 90°, indicating the dominance of salinity on the density. During this time, the use of isotherms as a proxy for isopycnals may lead to errors in our finescale estimates.

Figures 13 and 14 show the finescale-derived diffusivity for the upper 500 m of the water column, along with the strain ratio and shear utilized for the diffusivity estimates. At both moorings, the diffusivity is typically at or below our estimated noise floor of $\sim 10^{-6}\,\mathrm{m^2\,s^{-1}}$; however, there are several periods indicating elevated dissipation between 100 and 400 m. At N1, the subsurface shear is elevated for the duration of the SMC (July–September), and the diffusivity is not elevated above background levels until increased straining due to the background eddy field in October when turbulent mixing becomes strongest at the depth of the MicroMoor. It should be noted that there are several other events of similar magnitude that occur at other depths that do not seem to be associated with the presence of an eddy. For the purpose of this paper, we choose to focus on the vicinity of the MicroMoors, because at those locations, we have microstructure data to compare with our finescale estimates. To examine the relative contributions of strain and shear to mixing, we compare the frequency spectra of the layer averaged shear (Figs. 15a,c) and strain (Figs. 15b,d) at N1. These averages were calculated from shear and strain estimates between 120 and 140 m that were close to the depth of the MicroMoor. The top two subplots (Figs. 15a,b) represent shear and strain spectra taken during a period of increased mixing, that is between 15 September and 29 October 2018. Subplots in Figs. 15c and 15d show spectra evaluated between 15 November and 29 December 2018, which was a time of relative quiescence. We note a broadband increase in both shear and strain during the period of increased mixing. Total shear and strain variance increased by 49% and 43%, respectively, when integrated across all frequencies during the period of the increased mixing. When viewed as individual frequency bands, there was 135% increase in strain variance and an 85% increase in shear variance at subinertial frequencies. Subinertial strain accounted for 9% of the total variance during the quiescent time period, and 35% of the total variance during the passage of the eddy. Additionally, there was a 73% increase in shear variance between $0.8f$ and $1.2f$, and during both time periods this near-inertial frequency band contained ~10% of the total shear variance. Wijesekera et al. (2019) examined both shear and strain variance in a similar area between December 2013 and August 2015. During anticyclonic eddies, Wijesekera et al. (2019) found shear variance to be elevated by between 50% or by a factor of 2, and during cyclonic eddies, strain variance was found to be elevated by over a factor of 2, particularly in the semidiurnal band. Although we found slightly more enhancement of strain during an anticyclonic eddy, these results reinforce the idea that strain, shear, and subsequent turbulent mixing are highly influenced by the background eddy field in the southern BoB. Figure 16 compares diffusivities calculated using shear and temperature microstructure, with diffusivities estimated from finescale parameterizations averaged over a 40-m window surrounding the depth of the MicroMoor. Although the finescale parameterizations appear to underestimate the magnitude of turbulent mixing, both microstructure measurements and finescale estimates show that intermittent ~30-day events such as the one observed in October dominate the yearly mixing budget. Measurements at N1 suggest that for most of the year, turbulence is relatively weak, resulting in diapycnal diffusivities near those of molecular diffusion. Our shear based estimates of diffusivity are made only at high relative flow

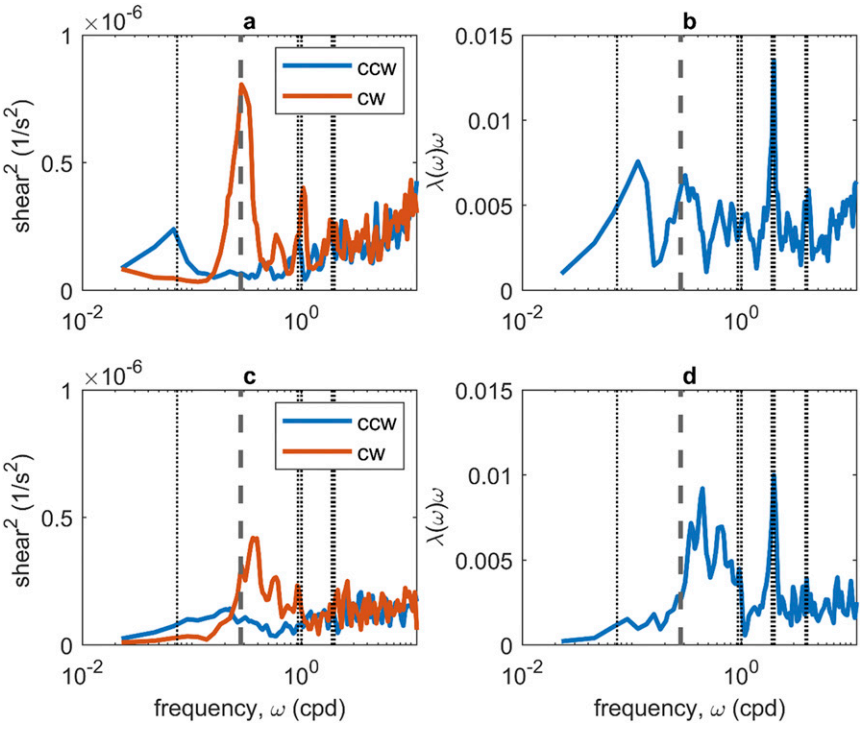


FIG. 15. Variance preserving (a),(c) shear and (b),(d) strain spectra at N1 averaged between 120 and 140 m. (top) The spectra calculated from shear and strain estimates during the passage of an anticyclonic eddy (15 Sep–29 Oct 2018). (bottom) Shear and strain spectra calculated for a period of low eddy activity (15 Nov–29 Dec 2018). The vertical black lines (from left to right) indicate spring–neap, inertial, diurnal ($K_1$, $O_1$), and semidiurnal ($M_2$, $S_2$) periods, and in (c) and (d) the first harmonic semidiurnal overtide are also shown.

velocities and thus likely represent an overestimate of total mixing. Conversely, our temperature microstructure based diffusivity estimates likely represent an underestimate. However, if we use both estimates together to estimate the average diffusivity over the whole record, the 11-month average is $\sim 10^{-4}\,\mathrm{m^2\,s^{-1}}$, indicating the importance of relatively infrequent eddy events and their interactions with finescale motions to drive the mixing within the BoB.

At N5, as at N1, turbulence appears to be intermittent, with prolonged periods of quiescence punctuated by large mixing events. At N5 (Fig. 11), values of temperature variance dissipation are largely below $\chi_T = 10^{-9}\,^\circ\mathrm{C^2\,s^{-1}}$ with elevated peaks during July, September–October (possibly corresponding to the anticyclonic eddy during September and October, Figs. 6 and 7), and in January (associated with a low-frequency downwelling event or anticyclonic eddy, Figs. 6 and 7). During periods of isotherm upcropping, the subsurface strain field at N5 becomes elevated (middle panel in Fig. 14). At these times high-turbulence levels are observed at the MicroMoor depth. During the event in October, the energetic anticyclonic eddy propagated west into the region of N5, which coincided with the northward movement of the SLD. Figure 17 (as in Fig. 16 but for N5) shows diffusivity estimates from both shear and temperature microstructure, along with diffusivity estimated from finescale parameterizations at the depth of the MicroMoor. In this case, finescale parameterizations appear to overestimate the magnitude of turbulent mixing; however, all diffusivity estimates agree in that both microstructure measurements and finescale estimates show that a few isolated events, within the upper 200 m, dominate the mixing over the course of the deployment.

### c. *Estimates of vertical turbulent heat and salinity flux*

Using our microstructure estimates of diffusivity, we follow the methodology of Cherian et al. (2020) to examine the relative importance of turbulent mixing to the seasonal cycle of heat and salt fluxes. Heat flux $J_q^t$ and salt flux $J_s^t$ are estimated from our dissipation time series using

$$J_q^t = -\rho_0 c_p K_T T_z, \tag{9}$$

$$J_s^t = -\rho_0 K_s S_z, \tag{10}$$

where $c_p$ is the heat capacity of seawater, $K_T$ and $K_s$ are the eddy diffusivities for temperature and salinity, $T_z$ is the local vertical temperature gradient, and $S_z$ is the local vertical salinity gradient, and $\rho_0$ is the density seawater. As in Cherian et al. (2020), we made the assumption that turbulence mixes all scalars at the same rate so that the turbulent diffusivities of both temperature and salinity are equal, and that $K_T = K_\rho$. This allows us to use both shear

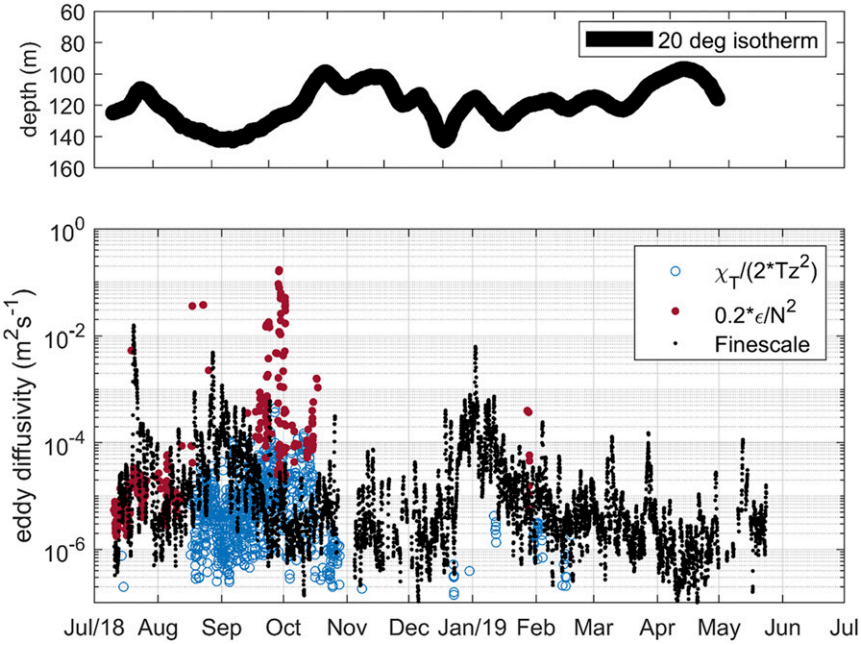


FIG. 16. Low-frequency background variability shown with (top) the 20° isotherm and (bottom) long-term estimates of diffusivity using the MicroMoor microstructure data derived $\chi_T$ and $\varepsilon$ values at N1 along with diffusivity estimates calculated from the finescale parameterization shown as black dots. Estimated diffusivities lower than molecular diffusion are not shown.

and temperature microstructure to estimate long-term salinity and heat flux at both N1 and N5.

Figures 18 and 19 show hourly averaged salt flux (top panels), heat flux (middle panels), and the cumulative sum of salt and heat flux (bottom panels) derived from shear and temperature microstructure. At N1, the highest values of both salt and heat flux occur during the anticyclonic eddy in October. At this time, about 10% of the data exceeds $5 \times 10^{-5}$ psu m s$^{-1}$, and

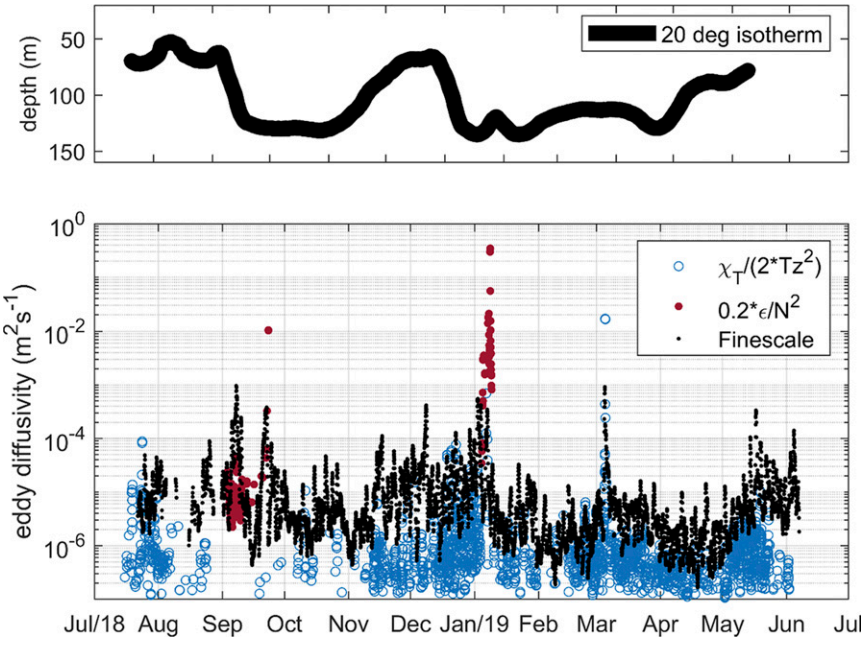


FIG. 17. As in Fig. 16, but for N5.

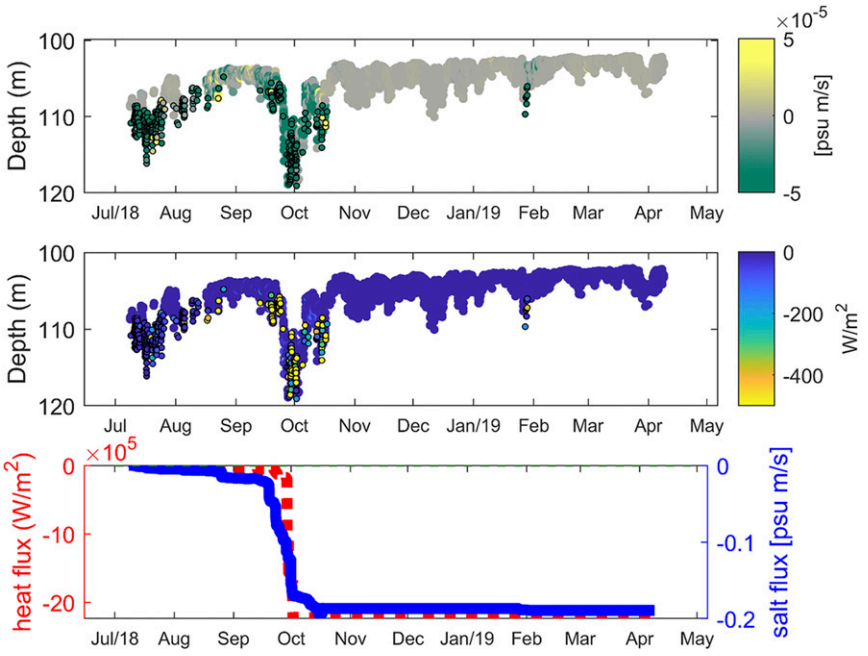


FIG. 18. Long-term estimates of the (top) salt flux and (middle) heat flux at mooring N1. (bottom) The cumulative sum of the heat flux (dashed red line) and salt flux (solid blue line). The largest markers (top two panels) show fluxes derived diffusivities obtained from temperature based microstructure, while smaller colored markers outlined in black are overlaid showing shear-based diffusivity estimates when available. In the top two plots, the MicroMoor depth is plotted on the $y$ axis to provide reference to the background conditions.

the 10-min averages of the salinity flux values reach $\sim 10^{-1}$ psu m s$^{-1}$. The monthly average of the salinity flux over the course of this event is $\sim 5 \times 10^{-6}$ psu m s$^{-1}$. During this time, 10% of 10-min averages of the heat flux exceed 5 W m$^{-2}$, while maximum heat flux values exceed 100 W m$^{-2}$, and daily averages peak above 20 W m$^{-2}$. These values appear to be larger than those reported in Cherian et al. (2020) by about a factor of 2. For both salinity and heat, the time period during September–October is responsible for over 90% of the total fluxes observed during the mooring deployment. At N5, the highest values of both salt and heat flux occur during the transition from negative to positive SSH anomaly in January. This transition of SSH anomaly may indicate that the mooring is located near the edge of a cyclonic eddy (or remnants of the SLD) during this time period. Over this period, instantaneous salinity flux values reach $\sim 10^{-3}$ psu m s$^{-1}$, while the monthly average of the salinity flux over the course of the January mixing event is $\sim 5 \times 10^{-7}$ psu m s$^{-1}$, about a factor of 10 smaller than the values seen at N1. The same is true for the cumulative flux values displayed in the bottom panels of Figs. 18 and 19. At N5, instantaneous heat flux values exceed 100 W m$^{-2}$, and daily averages reach 10 W m$^{-2}$ during the strongest mixing. Similarly to N1, the bulk of the total flux for both salinity and heat occurs in a few short isolated events.

## 5. Conclusions

Long-term observations of turbulence in the thermocline at two locations in the southern BoB were made using both moored microstructure measurements and finescale parameterizations of strain and shear. These observations span the period of July 2018–June 2019. The locations of these moorings allow for insight into subsurface mixing during the annual cycle of the Indian Ocean monsoon. At times, the microstructure and finescale estimates of turbulence show similar broad patterns and magnitudes, and at other times both estimates disagree by orders of magnitude. Furthermore, the data presented in this paper revealed a pattern of turbulent mixing linked to both the background eddy field, and high-frequency motions. At N1 (8°N, 85.75°E), we observed the passage of an anticyclonic eddy, which contained a particularly energetic subsurface flow to a depth of 200 m during October 2018. During this period, we also observed increases in high-frequency KE which coincided with heightened-turbulence levels. We found that at the depth of the MicroMoor, the bulk of the turbulent mixing during the yearlong record occurred at that time. At N5 (8°N, 83.75°E), the low-frequency field was dominated by alternating cyclonic and anticyclonic motions as the SLD moved from south to the north. Times of elevated turbulence appeared to coincide with transitions between these background flow regimes. Our main inferences are as follows:

1) Throughout much of the year, diffusivity in the southern BoB was low, i.e., $K_\rho \sim 10^{-6}$ m$^2$ s$^{-1}$ or below, both within the SMC and SLD. This finding agrees with the bulk of previous studies (Cherian et al. 2020; St. Laurent and Merrifield 2017). However, during the period of the mooring deployment, several significant mixing events were observed that are

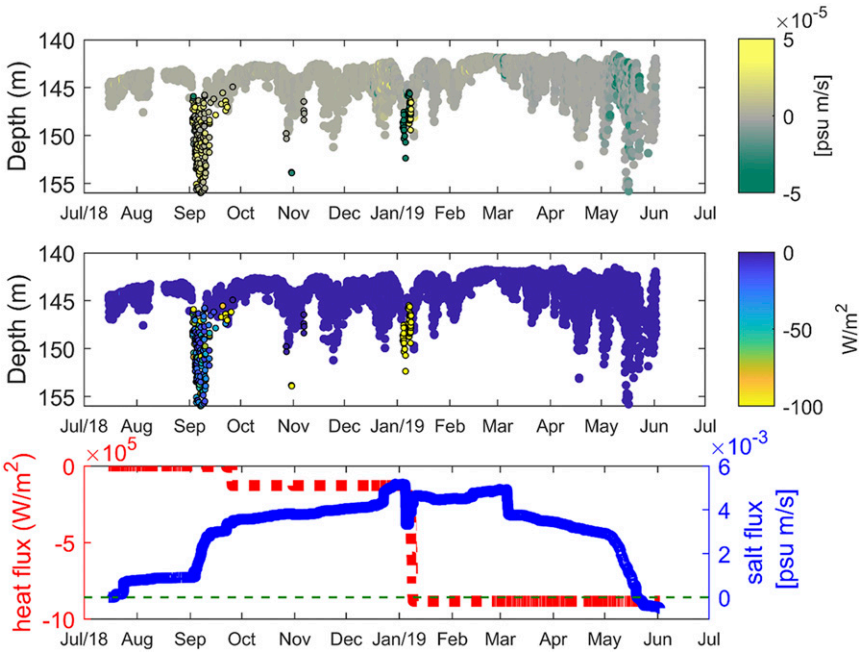


FIG. 19. As in Fig. 18, but for N5.

associated with much-higher diffusivity values above $\sim 10^{-3}\,m^2\,s^{-1}$, resulting in overall yearly averaged diffusivities near $\sim 10^{-4}\,m^2\,s^{-1}$.

2) Lozovatsky et al. (2019) reported weak diffusivities ($<10^{-5}\,m^2\,s^{-1}$) within the interior of the SLD but numerous patches of turbulence with diffusivities above $\sim 10^{-5}\,m^2\,s^{-1}$ at the dome's periphery. This is consistent with our findings, especially at N5. During periods of transition from positive to negative SSH anomaly, the edge of the SLD was collocated with the mooring. At these times, we observed elevated eddy diffusivities between $\sim 10^{-5}$ and $\sim 10^{-3}\,m^2\,s^{-1}$.
3) The increase and deepening of strain and shear fields that correspond with elevated turbulence during the passages of mesoscale eddies suggests that the low-frequency modification of the background field is a key ingredient for the generation of enhanced subsurface turbulence in the southern BoB. Intensification of both strain and horizontal shears generated by mesoscale eddies such as the SLD could lead to elevated turbulence and mixing compared to areas of low mesoscale activity as shown by the dramatic increase in low-frequency strain during the passage of an anticyclone eddy, along with the overall broadband increase in both strain and shear variance during that time. Furthermore, near-inertial, diurnal, and semidiurnal kinetic energies were elevated during times of increased turbulent mixing within the anticyclonic eddy. This suggests that dynamic interactions between the internal–gravity wave field and the eddy are crucial contributors to turbulent mixing.

Energetic mixing events in the southern BoB appear to occur in isolated, short-lived bursts. Although the particular mechanisms leading to the generation of turbulence are quite complicated, this dataset yields several key insights into the nature of turbulent mixing within the BoB. Turbulent mixing was strongly linked with the passage of mesoscale eddies/Rossby waves. Analyses of the low-frequency motions at both N1 and N5 show a link between the eddy field and dissipation levels. Low-frequency flows such as Rossby waves are a ubiquitous feature within the BoB, and have been shown to have seasonal cycles (Webber et al. 2018). One can speculate that the subsurface mixing cycles within the BoB are linked with the seasonality of these events, and thereby modulated by a combination of local forcing such as wind stress curl over the SLD, and remote equatorial forcing via Kelvin and Rossby wave propagation. However, without multiyear records of mixing, this conclusion is somewhat speculative. In general, we observed broadband high-frequency variabilities in temperature variance and kinetic energy that coincide with periods of enhanced turbulent mixing, with heightened finescale energy at near-inertial, diurnal, and semidiurnal frequencies. Examination of the turbulent salt and heat fluxes showed that for much of the year, the fluxes were low; however, during a small number of events linked to both the background eddy field and high-frequency motions, isolated mixing contributed substantially to the long-term turbulent fluxes. In short, eddies and their interactions with higher-frequency motions are critical to turbulent mixing within the BoB.

*Acknowledgments.* This work was sponsored by the U.S. Naval Research Laboratory project, "Role of Indian Ocean on Monsoon Intraseasonal Oscillation (RIO-MISO)," and the U.S. Office of Naval Research (ONR) in an ONR Departmental Research Initiative (DRI), "Monsoon Intraseasonal Oscillations in the Bay of Bengal (MISO-BOB)." H. J. S. Fernando was

funded by the ONR Grant N00014-17-1-2334. Special thanks to Andrew Quaid and Ian Martens for their efforts in preparation, deployment, and recovery of the moorings. The authors thank the captains and crews of the R/V *Thomas G. Thompson* and R/V *Sally Ride*. We additionally thank the two anonymous reviewers for their helpful comments and suggestions. The data used in this manuscript are archived by the Navy Research Laboratory at the Stennis Space Center. The corresponding author can be contacted for information to access the archived data.

## REFERENCES

Batchelor, G. K., 1959: Small-scale variation of convected quantities like temperature in turbulent fluid. *J. Fluid Mech.*, **5**, 113–133, https://doi.org/10.1017/S002211205900009X.

Bhat, G. S., and Coauthors, 2001: BOBMEX: The Bay of Bengal Monsoon Experiment. *Bull. Amer. Meteor. Soc.*, **82**, 2217–2243, https://doi.org/10.1175/1520-0477(2001)082<2217:BTBOBM>2.3.CO;2.

Chen, G., W. Han, Y. Li, M. J. McPhaden, J. Chen, W. Wang, and D. Wang, 2017: Strong intraseasonal variability of meridional currents near 5°N in the eastern Indian Ocean: Characteristics and causes. *J. Phys. Oceanogr.*, **47**, 979–998, https://doi.org/10.1175/JPO-D-16-0250.1.

Cherian, D. A., E. L. Shroyer, H. W. Wijesekera, and J. N. Moum, 2020: The seasonal cycle of upper-ocean mixing at 8°N in the Bay of Bengal. *J. Phys. Oceanogr.*, **50**, 323–342, https://doi.org/10.1175/JPO-D-19-0114.1.

Cullen, K. E., and E. L. Shroyer, 2019: Seasonality and interannual variability of the Sri Lanka dome. *Deep-Sea Res. II*, **168**, 104642, https://doi.org/10.1016/j.dsr2.2019.104642.

Dillon, T. M., and D. R. Caldwell, 1980: The Batchelor spectrum and dissipation in the upper ocean. *J. Geophys. Res.*, **85**, 1910–1916, https://doi.org/10.1029/JC085iC04p01910.

Goodman, L., E. R. Levine, and R. G. Lueck, 2006: On measuring the terms of the turbulent kinetic energy budget from an AUV. *J. Atmos. Oceanic Technol.*, **23**, 977–990, https://doi.org/10.1175/JTECH1889.1.

Gregg, M. C., 1989: Scaling turbulent dissipation in the thermocline. *J. Geophys. Res.*, **94**, 9686–9698, https://doi.org/10.1029/JC094iC07p09686.

——, and T. B. Sanford, 1988: The dependence of turbulent dissipation on stratification in a diffusively stable thermocline. *J. Geophys. Res.*, **93**, 12 381–12 392, https://doi.org/10.1029/JC093iC10p12381.

——, E. A. D'Asaro, J. J. Riley, and E. Kunze, 2018: Mixing efficiency in the ocean. *Annu. Rev. Marine Sci.*, **10**, 443–473, https://doi.org/10.1146/annurev-marine-121916-063643.

Jensen, T. G., H. W. Wijesekera, E. S. Nyadjro, P. G. Thoppil, J. F. Shriver, K. K. Sandeep, and V. Pant, 2016: Modeling salinity exchanges between the equatorial Indian Ocean and the Bay of Bengal. *Oceanography*, **29** (2), 92–101, https://doi.org/10.5670/oceanog.2016.42.

——, J. Magalhães, H. W. Wijesekera, M. Buijsman, R. Helber, and J. Richman, 2020: Numerical modelling of tidally generated internal wave radiation from the Andaman Sea into the Bay of Bengal. *Deep-Sea Res. II*, **172**, 104710, https://doi.org/10.1016/j.dsr2.2019.104710.

Jinadasa, S. U. P., I. Lozovatsky, J. Planella-Morató, J. D. Nash, J. A. MacKinnon, A. J. Lucas, H. W. Wijesekera, and H. J. S. Fernando, 2016: Ocean turbulence and mixing around Sri Lanka and in adjacent waters of the northern Bay of Bengal. *Oceanography*, **29** (2), 170–179, https://doi.org/10.5670/oceanog.2016.49.

Kumar, B. P., J. Vialard, M. Lengaigne V. S. N. Murty, and M. J. McPhaden, 2012: TropFlux: Air-sea fluxes for the global tropical oceans—Description and evaluation. *Climate Dyn.*, **38**, 1521–1543, https://doi.org/10.1007/s00382-011-1115-0.

Kunze, E., 2017: Internal-wave-driven mixing: Global geography and budgets. *J. Phys. Oceanogr.*, **47**, 1325–1345, https://doi.org/10.1175/JPO-D-16-0141.1.

——, R. W. Schmitt, and J. M. Toole, 1995: The energy balance in a warm-core ring's near-inertial critical layer. *J. Phys. Oceanogr.*, **25**, 942–957, https://doi.org/10.1175/1520-0485(1995)025<0942:TEBIAW>2.0.CO;2.

——, E. Firing, J. M. Hummon, T. K. Chereskin, and A. M. Thurnherr, 2006: Global abyssal mixing inferred from lowered ADCP shear and CTD strain profiles. *J. Phys. Oceanogr.*, **36**, 1553–1576, https://doi.org/10.1175/JPO2926.1.

Lozovatsky, I., H. Wijesekera, E. Jarosz, M.-J. Lilover, A. Pirro, Z. Silver, L. Centurioni, and H. J. S. Fernando, 2016: A snapshot of internal waves and hydrodynamic instabilities in the southern Bay of Bengal. *J. Geophys. Res. Oceans*, **121**, 5898–5915, https://doi.org/10.1002/2016JC011697.

——, A. Pirro, E. Jarosz, H. W. Wijesekera, S. U. P. Jinadasa, and H. J. S. Fernando, 2019: Turbulence at the periphery of Sri Lanka dome. *Deep-Sea Res. II*, **168**, 104614, https://doi.org/10.1016/j.dsr2.2019.07.002.

Lueck, R. G., 2016: Calculating the rate of dissipation of turbulent kinetic energy. Rockland Scientific International Tech. Note 028, 19 pp., https://rocklandscientific.com/support/knowledge-base/technical-notes/.

——, F. Wolk, J. Hancyck, and K. Black, 2015: Hub-height time series measurements of velocity and dissipation of turbulence kinetic energy in a tidal channel, *IEEE/OES 11th Current, Waves and Turbulence Measurement*, St. Petersburg, FL, IEEE, https://doi.org/10.1109/CWTM.2015.7098143.

Moum, J. N., and J. D. Nash, 2009: Mixing measurements on an equatorial ocean mooring. *J. Atmos. Oceanic Technol.*, **26**, 317–336, https://doi.org/10.1175/2008JTECHO617.1.

Nasmyth, P. W., 1970: Oceanic turbulence. Ph.D. thesis, Institute of Oceanography, University of British Columbia, 106 pp.

Osborn, T. R., 1974: Vertical profiling of velocity microstructure. *J. Phys. Oceanogr.*, **4**, 109–115, https://doi.org/10.1175/1520-0485(1974)004<0109:VPOVM>2.0.CO;2.

——, 1980: Estimates of the local rate of vertical diffusion from dissipation measurements. *J. Phys. Oceanogr.*, **10**, 83–89, https://doi.org/10.1175/1520-0485(1980)010<0083:EOTLRO>2.0.CO;2.

——, and C. S. Cox, 1972: Oceanic fine structure. *Geophys. Fluid Dyn.*, **3**, 321–345, https://doi.org/10.1080/03091927208236085.

Pirro, A., H. J. S. Fernando, H. W. Wijesekera, T. G. Jensen, L. R. Centurioni, and S. U. P. Jinadasa, 2020a: Eddies and currents in the Bay of Bengal during summer monsoons. *Deep-Sea Res. II*, **172**, 104728, https://doi.org/10.1016/j.dsr2.2019.104728.

——, H. W. Wijesekera, E. Jarosz, and H. J. S. Fernando, 2020b: Dynamics of intraseasonal oscillations in the Bay of Bengal during summer monsoons captured by mooring observations. *Deep-Sea Res. II*, **172**, 104718, https://doi.org/10.1016/j.dsr2.2019.104718.

Polzin, K. L., 2010: Mesoscale eddy–internal wave coupling. Part II: Energetics and results from PolyMode. *J. Phys. Oceanogr.*, **40**, 789–801, https://doi.org/10.1175/2009JPO4039.1.

——, J. M. Toole, and R. W. Schmitt, 1995: Finescale parameterizations of turbulent dissipation. *J. Phys. Oceanogr.*, **25**, 306–328,

https://doi.org/10.1175/1520-0485(1995)025<0306:FPOTD>2.0.CO;2.

Rao, S. A., and Coauthors, 2011: Modulation of SST, SSS over northern Bay of Bengal on ISO time scale. *J. Geophys. Res.*, **116**, C09026, https://doi.org/10.1029/2010JC006804.

Ruddick, B., 1983: A practical indicator of the stability of the water column to double-diffusive activity. *Deep-Sea Res.*, **30**, 1105–1107, https://doi.org/10.1016/0198-0149(83)90063-8.

Schott, F., and J. P. McCreary, 2001: The monsoon circulation of the Indian Ocean. *Prog. Oceanogr.*, **51**, 1–123, https://doi.org/10.1016/S0079-6611(01)00083-0.

St. Laurent, L., and S. Merrifield, 2017: Measurements of near-surface turbulence and mixing from autonomous ocean gliders. *Oceanography*, **30** (2), 116–125, https://doi.org/10.5670/oceanog.2017.231.

Thakur, R., E. L. Shroyer, R. Govindarajan, J. T. Farrar, R. A. Weller, and J. N. Moum, 2019: Seasonality and buoyancy suppression of turbulence in the Bay of Bengal. *Geophys. Res. Lett.*, **46**, 4346–4355, https://doi.org/10.1029/2018GL081577.

Torrence, C., and G. P. Compo, 1998: A practical guide to wavelet analysis. *Bull. Amer. Meteor. Soc.*, **79**, 61–78, https://doi.org/10.1175/1520-0477(1998)079<0061:APGTWA>2.0.CO;2.

Vinayachandran, P. N., and T. Yamagata, 1998: Monsoon response of the sea around Sri Lanka: Generation of thermal domes and anticyclonic vortices. *J. Phys. Oceanogr.*, **28**, 1946–1960, https://doi.org/10.1175/1520-0485(1998)028<1946:MROTSA>2.0.CO;2.

——, D. Shankar, S. Vernekar, K.K. Sandeep, P. Amol, C.P. Neema, and A. Chatterjee, 2013: A summer monsoon pump to keep the Bay of Bengal salty. *Geophys. Res. Lett.*, **40**, 1777–1782, https://doi.org/10.1002/grl.50274.

——, and Coauthors, 2018: BOBBLE: Ocean–atmosphere interaction and its impact on the South Asian monsoon. *Bull. Amer. Meteor. Soc.*, **99**, 1569–1587, https://doi.org/10.1175/BAMS-D-16-0230.1.

Warner, S. J., J. Becherer, K. Pujiana, E. L. Shroyer, M. Ravichandran, V. P. Thangaprakash, and J. N. Moum, 2016: Monsoon mixing cycles in the Bay of Bengal: A year-long subsurface mixing record. *Oceanography*, **29** (2), 158–169, https://doi.org/10.5670/oceanog.2016.48.

Webber, B. G. M., A. J. Matthews, P. N. Vinayachandran, C. P. Neema, A. Sanchez-Franks, V. Vijith, P. Amol, and D. B. Baranowski, 2018: The dynamics of the Southwest Monsoon Current in 2016 from high-resolution in situ observations and models. *J. Phys. Oceanogr.*, **48**, 2259–2282, https://doi.org/10.1175/JPO-D-17-0215.1.

Webster, P. J., and Coauthors, 2002: The JASMINE pilot study. *Bull. Amer. Meteor. Soc.*, **83**, 1603–1630, https://doi.org/10.1175/BAMS-83-11-1603.

Whalen, C. B., J. A. MacKinnon, L. D. Talley, and A. F. Waterhouse, 2015: Estimating the mean diapycnal mixing using a finescale strain parameterization. *J. Phys. Oceanogr.*, **45**, 1174–1188, https://doi.org/10.1175/JPO-D-14-0167.1.

Wijesekera, H., L. Padman, T. Dillon, M. Levine, C. Paulson, and R. Pinkel, 1993: The application of internal-wave dissipation models to a region of strong mixing. *J. Phys. Oceanogr.*, **23**, 269–286, https://doi.org/10.1175/1520-0485(1993)023<0269:TAOIWD>2.0.CO;2.

——, and Coauthors, 2016a: ASIRI: An ocean–atmosphere initiative for Bay of Bengal. *Bull. Amer. Meteor. Soc.*, **97**, 1859–1884, https://doi.org/10.1175/BAMS-D-14-00197.1.

——, W. J. Teague, D. W. Wang, E. Jarosz, and T. G. Jenson, 2016b: Low-frequency currents from deep moorings in the southern Bay of Bengal. *J. Phys. Oceanogr.*, **46**, 3209–3238, https://doi.org/10.1175/JPO-D-16-0113.1.

Wijesekera, H. W., W. J. Teague, E. Jarosz, D. W. Wang, H. J. S. Fernando, and Z. R. Hallock, 2019: Internal tidal currents and solitons in the southern Bay of Bengal. *Deep-Sea Res. II*, **168**, 104587, https://doi.org/10.1016/j.dsr2.2019.05.010.

Wolk, F., H. Yamazaki, L. Seuront, and R. G. Lueck, 2002: A new free-fall profiler for measuring biophysical microstructure. *J. Atmos. Oceanic Technol.*, **19**, 780–793, https://doi.org/10.1175/1520-0426(2002)019<0780:ANFFPF>2.0.CO;2.